# Accelerated evolution of convective simulations

Evan H. Anders and Benjamin P. Brown

*Dept. Astrophysical & Planetary Sciences, University of Colorado – Boulder, Boulder, CO 80309, USA and*
*Laboratory for Atmospheric and Space Physics, Boulder, CO 80303, USA*

Jeffrey S. Oishi

*Department of Physics and Astronomy, Bates College, Lewiston, ME 04240, USA*

We present a method for achieving Accelerated Evolution (AE) of convective simulations. By probing the dynamics of convection early in simulations and adjusting the thermal profile of the simulation appropriately, we advance simulations to evolved states on timescales much shorter than the thermal diffusion timescale. We study this method in the context of Rayleigh-Bénard convection. The solutions reached by AE similar to those reached by a slow thermal evolution, and AE is effective in 2D, 3D, and at low and high supercriticality. Extensions to more complex systems are briefly discussed.

## I. INTRODUCTION

Natural convection occurs in the presence of disparate timescales which prohibit numericists from studying realistic models of systems in nature. For example, flows in the convection zones of stars like the Sun are characteristically low Mach number (Ma) in the deep interior. Explicit timestepping methods which are bound by the Courant-Friedrich-Lewy (CFL) timestep limit must resolve the fastest motions (sound waves), resulting in timesteps which are prohibitively small for studies of the deep, low-Ma motions. These systems are numerically stiff, and the difference between the sound crossing time and the convective overturn time have made studies of low-Ma stellar convection difficult. Traditionally, approximations such as the anelastic approximation, in which sound waves are explicitly filtered out, have been used to study low-Ma flows [1, 2]. More recently, advanced numerical techniques which use implicit or mixed implicit-explicit timestepping mechanisms have made it feasible to study convection at low Mach numbers [3–8], and careful studies of deep convection which would have been impossible a decade ago are now widely accessible.

Unfortunately, convective systems generally evolve over the course of thermal timescales, which are often much larger than dynamical timescales. Therefore resolving dynamics in atmospheres which are sufficiently thermally relaxed remains a challenging problem. Solar convection is a prime example of this phenomenon, as dynamical timescales in the solar convective zone are relatively short (convection overturns every $\sim 10$ minutes at the solar surface, the Sun rotates roughly once every month) compared to the Sun's Kelvin-Helmholtz timescale of $3 \cdot 10^7$ years [9]. In such a system, it is impossible to resolve the convective dynamics while also meaningfully evolving the thermal structure of the system using traditional timestepping techniques alone. As modern simulations aim to model natural convection by increasing into the high-Rayleigh-number (Ra) regime, the thermal diffusion timescale becomes intractably large compared to dynamical timescales [7]. Furthermore, as dynamical and thermal timescales separate, simulations become more turbulent. Capturing appropriately resolved turbulent motions requires finer grid meshes and smaller timesteps. Thus, the progression of simulations into the high-Ra regime of natural convection is slowed by two simultaneous effects: timestepping through a single convective overturn time becomes more computationally expensive and the number of overturn times required for systems to reach thermal equilibration grows.

The vast difference between convective and thermal timescales has long plagued numericists studying convection, and an abundance of approaches has been employed to study thermally converged solutions. One popular method for accelerating the convergence of high-Ra solutions is by "bootstrapping" – the process of using the flow fields in a converged solution at low Ra as initial conditions for a simulation at high Ra. This method has been used with great success [10, 11], but it is not without its faults. Bootstrapped solutions are succeptible to hysteresis effects, in which large-scale convective structures present in the low Ra solution imprint onto the dynamics of the new, high Ra solution. Another commonly-used tactic in moderate-Ra simulations is to use a simple model of the full convective state as initial conditions. For example, past studies have used a linear eigenvalue solve to set the initial convective state [12] or used an axisymmetric solution as initial conditions for convection in a 3D cylinder [11]. In other systems, the approximate state of the evolved solution can be estimated. There, a set of initial conditions which is close to the evolved state can be derived analytically [13, 14].

Despite the numerous methods that have been used, the most straightforward way to achieve a thermally converged solution is to evolve a convective simulation through a thermal timescale. Some modern studies do just that [2]. However, such evolution is *expensive*, and state-of-the-art simulations at the highest values of Ra can only reasonably be run for tens to hundreds of freefall timescales [15], much less the thousands of freefall times required for thermal

convergence.

In this work, we study a method of achieving accelerated evolution of convective simulations. We couple measurements of the dynamics of non-converged convective simulations with knowledge about energy balances in the desired solution to self-consistently adjust the mean thermodynamic profile towards its evolved state. While such a method has been used previously [16], we find no explanation in the current literature of the steps involved in employing this method, nor any study into the accuracy of such a method. In section II, we describe our convective simulations, our numerical methods, and our method for achieving accelerated evolution. In section III, we compare accelerated evolution solutions to solutions obtained from evolution through a full thermal diffusion timescale. Finally, in section IV, we offer concluding remarks and discuss extensions of the methods presented here.

## II. EXPERIMENT

We study incompressible Rayleigh-Bénard convection under the Oberbeck-Boussinesq approximation, such that the fluid has a constant kinematic viscosity ($\nu$), thermal diffusivity ($\kappa$), and coefficient of thermal expansion ($\alpha$). The density of the fluid is a constant, $\rho_0$, except where it is $\rho = \rho_0(1 - \alpha T_1)$ on the term where the constant gravitational acceleration, $\boldsymbol{g} = -g\hat{z}$, acts in the vertical momentum equation. The equations of motion are [17]

$$\nabla \cdot \boldsymbol{u} = 0, \tag{1}$$

$$\frac{\partial \boldsymbol{u}}{\partial t} + \boldsymbol{u} \cdot \nabla \boldsymbol{u} = -\frac{1}{\rho_0}\nabla P - g(1 - \alpha T_1)\hat{z} + \nu\nabla^2\boldsymbol{u}, \tag{2}$$

$$\frac{\partial T_1}{\partial t} + \boldsymbol{u} \cdot \nabla(T_0 + T_1) = \kappa\nabla^2 T_1, \tag{3}$$

where $\boldsymbol{u} = u\hat{x} + v\hat{y} + w\hat{z}$ is the velocity, $T = T_0 + T_1$ are the initial and fluctuating components of temperature, and $P$ is the pressure. We non-dimensionalize these equations such that length is in units of the layer height ($L_z$), temperature is in units of the initial temperature jump across the layer ($\Delta T_0 = L_z\nabla T_0$), and velocity is in units of the freefall velocity ($v_{\text{ff}} = \sqrt{\alpha g L_z^2 \nabla T_0}$). By these choices, one time unit is a freefall time ($t_{\text{ff}} = L_z/v_{\text{ff}}$). We introduce a reduced kinematic pressure, $\varpi \equiv (P/\rho_0 + \phi + |\boldsymbol{u}|^2/2)/v_{\text{ff}}^2$, where the gravitational potential, $\phi$, is defined such that $\boldsymbol{g} = -\nabla\phi$. As $P$ is a Langrange multiplier under the Oberbeck-Boussinesq approximation, $\varpi$ can be treated straightforwardly as a linear variable. In non-dimensional form, Eqns. 2 & 3 become

$$\frac{\partial \boldsymbol{u}}{\partial t} + \nabla\varpi - T_1\hat{z} + \mathcal{R}\nabla \times \boldsymbol{\omega} = \boldsymbol{u} \times \boldsymbol{\omega}, \tag{4}$$

$$\frac{\partial T_1}{\partial t} - \mathcal{P}\nabla^2 T_1 + w\frac{\partial T_0}{\partial z} = -\boldsymbol{u} \cdot \nabla T_1, \tag{5}$$

where $\boldsymbol{\omega} = \nabla \times \boldsymbol{u}$ is the vorticity. The dimensionless control parameters $\mathcal{P}$ and $\mathcal{R}$ are set by the Rayleigh and Prandtl numbers,

$$\mathcal{R} \equiv \sqrt{\frac{\text{Pr}}{\text{Ra}}}, \qquad \mathcal{P} \equiv \frac{1}{\sqrt{\text{Pr}\,\text{Ra}}}, \qquad \text{Ra} = \frac{g\alpha L_z^4 \nabla T_0}{\nu\kappa} = \frac{(L_z\,v_{\text{ff}})^2}{\nu\kappa}, \qquad \text{Pr} = \frac{\nu}{\kappa}. \tag{6}$$

We hold Pr= 1 constant throughout this work, such that $\mathcal{P} = \mathcal{R}$.

We study 2D and 3D convection in which the domain is a cartesian box, whose dimensionless vertical extent is $z \in [-1/2, 1/2]$, and which is horizontally periodic with an extent of $x, y \in [0, \Gamma]$, where $\Gamma = 2$ is the aspect ratio. In 2D simulations, we set $v = \partial_y = 0$. We specify no-slip, impenetrable boundary conditions at both the top and bottom boundary and we use mixed thermal boundary conditions, such that

$$u = v = w = 0 \text{ at } z = \pm 1/2, \qquad T_1 = 0 \text{ at } z = +1/2, \qquad \frac{\partial T_1}{\partial z} = 0 \text{ at } z = -1/2. \tag{7}$$

For this choice of boundary conditions, the critical value of Ra at which the onset of convection occurs is $\text{Ra}_{\text{crit}} = 1295.78$, and the supercriticality of a run is defined as $S \equiv \text{Ra}/\text{Ra}_{\text{crit}}$. Studies of convection which aim to model astrophysical systems such as stars often employ mixed thermal boundary conditions [12, 18, 19], as we do here; however, our choice of thermal boundary conditions here reflects the fact that the conditions in Eqn. (7) are the simplest to implement in the process of accelerated evolution (see section II A) we study here.

We utilize the Dedalus[1] pseudospectral framework [20] to evolve Eqns. (1), (4), & (5) forward in time using an implicit-explicit (IMEX), third-order, four-step Runge-Kutta timestepping scheme RK443 [21]. The linear terms (on

---

[1] http://dedalus-project.org/

the LHS of the equations) are solved implicitly, while the nonlinear terms (RHS) are explicitly solved. Variables are time-evolved on a dealiased Chebyshev (vertical) and Fourier (horizontal, periodic) domain in which the physical grid dimensions are 3/2 the size of the coefficient grid.

As initial conditions, we fill $T_1$ with random white noise whose magnitude is $10^{-6}\mathcal{P}$. This ensures that the initial perturbations are much smaller than the evolved convective temperature perturbations, even at large Ra. We filter this noise spectrum in coefficient space, such that only the lower 25% of the coefficients have power.

## A.  The method of Accelerated Evolution

Here we describe a method of Accelerated Evolution (AE), which we use to rapidly evolve the thermodynamic state of convective simulations. We compare this AE method to Standard Evolution (SE), in which we naively evolve the atmosphere for one thermal diffusion time, $t_\kappa = \mathcal{P}^{-1}$. As Ra increases, SE solutions become intractable, while the timeframe of convergence for an AE solution remains nearly constant in freefall time units. For an example of time saving achieved by using AE, we compare energy traces at $S = 10^5$ from a SE run in Fig. 1a to an AE run in Fig. 1c.

The horizontally averaged profiles of the vertical conductive flux, $F_{\text{cond}} = \langle -\kappa\nabla(T_0 + T_1)\rangle_{x,y}$, and the vertical convective flux, $F_{\text{conv}} = \langle w(T_0 + T_1)\rangle_{x,y}$, are the basis of the AE method. Here we use $\langle\rangle_{x,y}$ to represent a horizontal average. We measure both of these fluxes early in a simulation, retrieving profiles such as those shown in Fig. 1b. At early stages in the simulation, these flux profiles are highly asymmetric, with more flux exiting the atmosphere at the upper boundary than the fixed-flux lower boundary is providing. By calculating the total flux, $F_{\text{tot}} = F_{\text{conv}} + F_{\text{cond}}$, we derive the profiles

$$f_{\text{conv}}(z) = \frac{F_{\text{conv}}}{F_{\text{tot}}}, \qquad f_{\text{cond}}(z) = \frac{F_{\text{cond}}}{F_{\text{tot}}}, \tag{8}$$

which have the systematic asymmetries removed. These profiles describe which parts of the atmosphere depend on convection to carry flux (where $f_{\text{conv}}(z) = 1$ and $f_{\text{cond}}(z) = 0$). We presume that the early convection occupies roughly the same volume as the evolved convection, and thus that the extent of the early thermal boundary layers (where $f_{\text{cond}}(z) = 1$ and $f_{\text{conv}}(z) = 0$) will not change significantly over the course of the atmosphere's evolution. Under this assumption, the proper evolved atmospheric flux profiles are $F_{\text{conv, ev}} = F_{\text{bot}} \cdot f_{\text{conv}}$ and $F_{\text{cond, ev}} = F_{\text{bot}} \cdot f_{\text{cond}}$, where $F_{\text{bot}} = \mathcal{P}$ is the amount of flux entering the bottom of the atmosphere.

In a time-stationary state, the horizontal- and time-average of Eqns. (4) and (5), neglecting terms which vanish due to symmetry, are

$$\frac{\partial}{\partial z}\langle\varpi\rangle_{x,y} - \langle T_1\rangle_{x,y}\,\hat{z} = \langle\boldsymbol{u}\times\boldsymbol{\omega}\rangle_{x,y}, \tag{9}$$

$$\frac{\partial}{\partial z}F_{\text{conv, ev}} - \mathcal{P}\frac{\partial^2}{\partial z^2}\langle T_1\rangle_{x,y} = 0. \tag{10}$$

Convective flows are perturbations around a thermal profile defined by these equations in the proper evolved, statistically stationary state. Furthermore, under the specification of $F_{\text{conv, ev}}$ and $\langle\boldsymbol{u}\times\boldsymbol{\omega}\rangle_{x,y}$, *the mean thermodynamic structure of the system is fully specified.*

Thus, the AE method is simple: we construct $F_{\text{conv, ev}}$ as described above. Then we calculate a profile, $\xi(z) = F_{\text{conv, ev}}/F_{\text{conv}}$, which is the fraction, as a function of height, by which the flux in the system must be reduced to go from an initial state (Fig. 1b) to an evolved state (Fig. 1d). We multiply the velocities and the thermal fluctuations, $T - \langle T\rangle_{x,y}$, by $\sqrt{\xi}$, such that the advected, flux-carrying perturbations in the temperature are appropriately diminished. We then solve a 1D boundary value problem including Eqns. (9) & (10) using $F_{\text{conv, ev}}$ and $\langle\boldsymbol{u}\times\boldsymbol{\omega}\rangle_{x,y}$, after diminishing it by a factor of $\xi$. We use mixed thermal boundary conditions in this study, as in Eqn. (7), because $F_{\text{bot}}$ is exactly specified, and the temperature profile is fixed at a reference value for the AE solve. For specifics on the precise implementation of the AE method, we refer the reader to appendix A.

The AE method converges atmospheres from extreme flux disequilibrium states (Fig. 1b) on short dynamical timescales (Fig. 1c) to a converged state (Fig. 1d) whose flux balance is very close to the balance present in the corresponding SE solution (Fig. 1e). While the application of the AE method advances solutions toward the proper solution, we find that multiple applications of the method is the best means of achieving converged solutions quickly.

## III.  RESULTS

We study evolved SE solutions in $S \in (1, 10^5]$ in 2D and $S \in (1, 10^4]$ in 3D. We compare their properties to accelerated evolution (AE) runs in $S \in (1, 10^7]$ in 2D and $S \in (1, 10^4]$ in 3D. We refer the reader to appendix B for a full list of simulations.
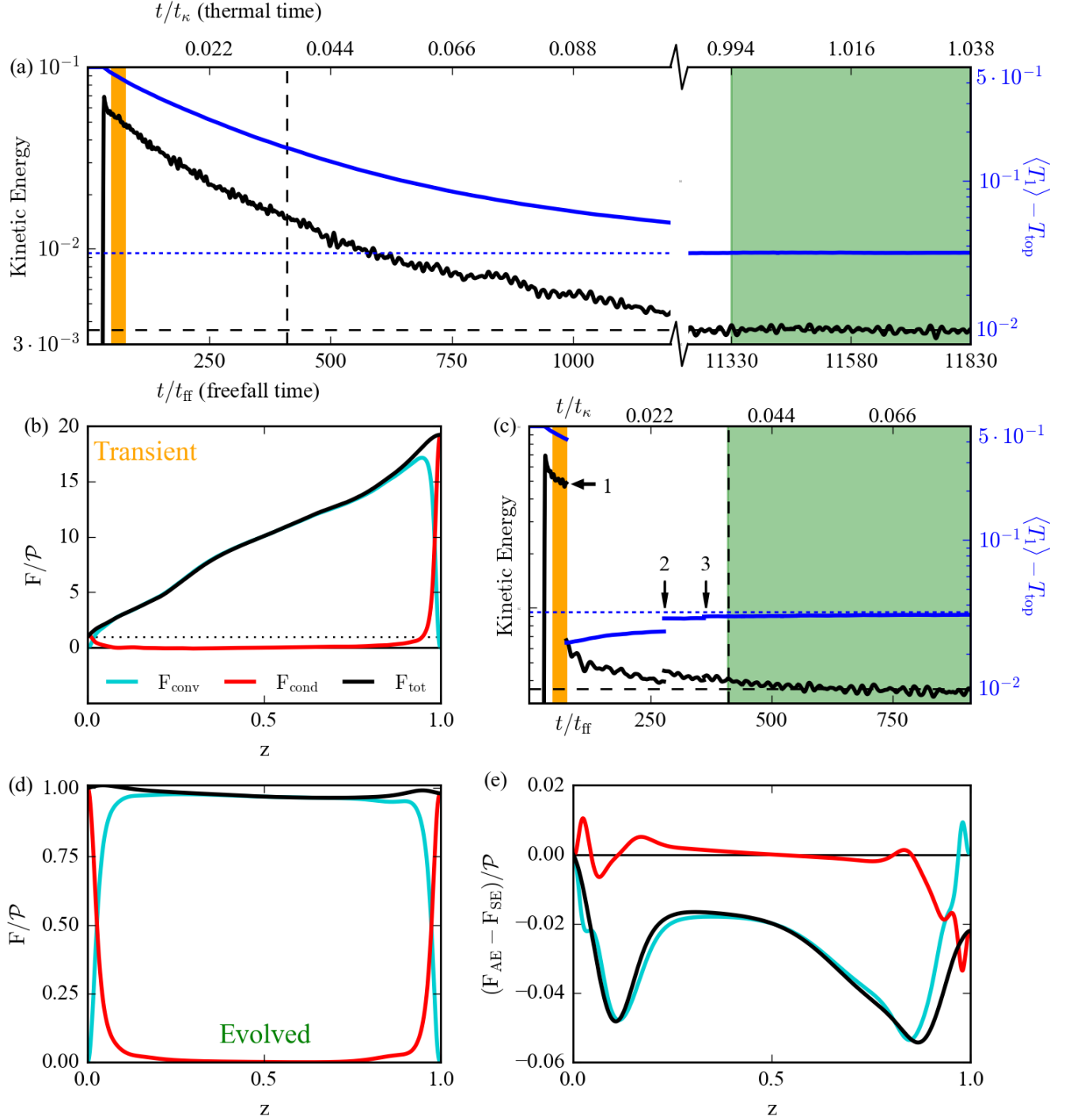
FIG. 1. (a) Kinetic energy (black) and mean temperature (blue) vs. time are shown for a SE run at $S = 10^5$. The mean evolved values of kinetic energy and mean temperature, averaged over the time shaded in green, are denoted by the horizontal dashed lines. (b) The time- and horizontally-averaged flux profiles are shown for the times highlighted in orange in (a). (c) The same quantities as in (a) are shown, but for AE at the same parameters. The axes are scaled identically in (a) and (c), and the AE method is used three times, marked by the numbered arrows in (c). The fluxes averaged over the green shaded region of (c) are shown in (d). The difference between the fluxes in the AE and SE solutions is shown in (e). The dashed vertical line in (a) and (c) denotes the simulation time at which evolved measurements are started for the AE case.

The time- and volume-averaged values of the Nusselt number (Nu), the RMS Reynolds number (Re), and the mean temperature in AE solutions are shown in Fig. 2a-c. Nu, which quantifies the heat transport in evolved solutions, is shown as a function of Ra and $S$ in Fig. 2a. Nu is defined as

$$\mathrm{Nu} = \frac{\langle F_{\mathrm{conv}} + F_{\mathrm{cond}} \rangle}{\langle F_{\mathrm{cond,\ ref}} \rangle} = \frac{\langle wT - \mathcal{P}\partial_z T \rangle}{\langle -\mathcal{P}\partial_z T \rangle}, \tag{11}$$

where the volume average of a quantity, $g$, is shown as $\langle g \rangle$. When $S < 10^{3+2/3}$ in 2D and for all runs in 3D, the evolved system is characterized by a specific value of Nu, as the convective heat transport reaches a temporally stationary state. At larger values of $S$ in 2D, the convective plumes consistently oscillate horizontally, leading to variations in Nu over time as the heat transport is alternately assisted and diminished by these oscillations. As a result of our choice of no-slip boundary conditions, the fluid never enters a full domain shearing state [22], and the oscillatory nature of the plumes is stable. The 2D SE simulations exhibit the same horizontally oscillatory behavior as the AE solutions for the same initial conditions. The dynamic nature of the plume structures diminishes the scaling of the heat transport to $\mathrm{Nu} \propto \mathrm{Ra}^{1/5}$, which is weaker than classic scaling laws [10, 23]. Previous studies in 2D convection may have avoided oscillatory plumes by using bootstrapping techniques as initial conditions for high $S$ runs.

In Fig. 2b, we report $\mathrm{Re} = \langle |\boldsymbol{u}| \rangle / \mathcal{R}$. This measures the degree of turbulence in the solution, and scales roughly as $\mathrm{Re} \propto \mathrm{Ra}^{0.45}$. Each simulation shows little variance in the value of Re over time.

Fig. 2c shows the scaling of $\langle T \rangle - T_{\mathrm{top}}$. The average temperature, $\langle T \rangle$, is dominated by its value in the isothermal interior, so this measurements serves as a probe of the temperature jump across the boundary layers. As a result, we expect this measure to scaling inversely with Nu in converged solutions where fixed-flux boundary conditions are used [24]. We find here that $(\langle T \rangle - T_{\mathrm{top}}) \propto \mathrm{Ra}^{-1/5}$, precisely the inverse scaling of Nu.

In Fig. 2d-f, we report the fractional difference between measurements in the AE and SE solutions. The mean values of Nu and $\langle T \rangle - T_{\mathrm{top}}$ measured in AE are accurate to SE values to within $\sim 1\%$. Re measurements show
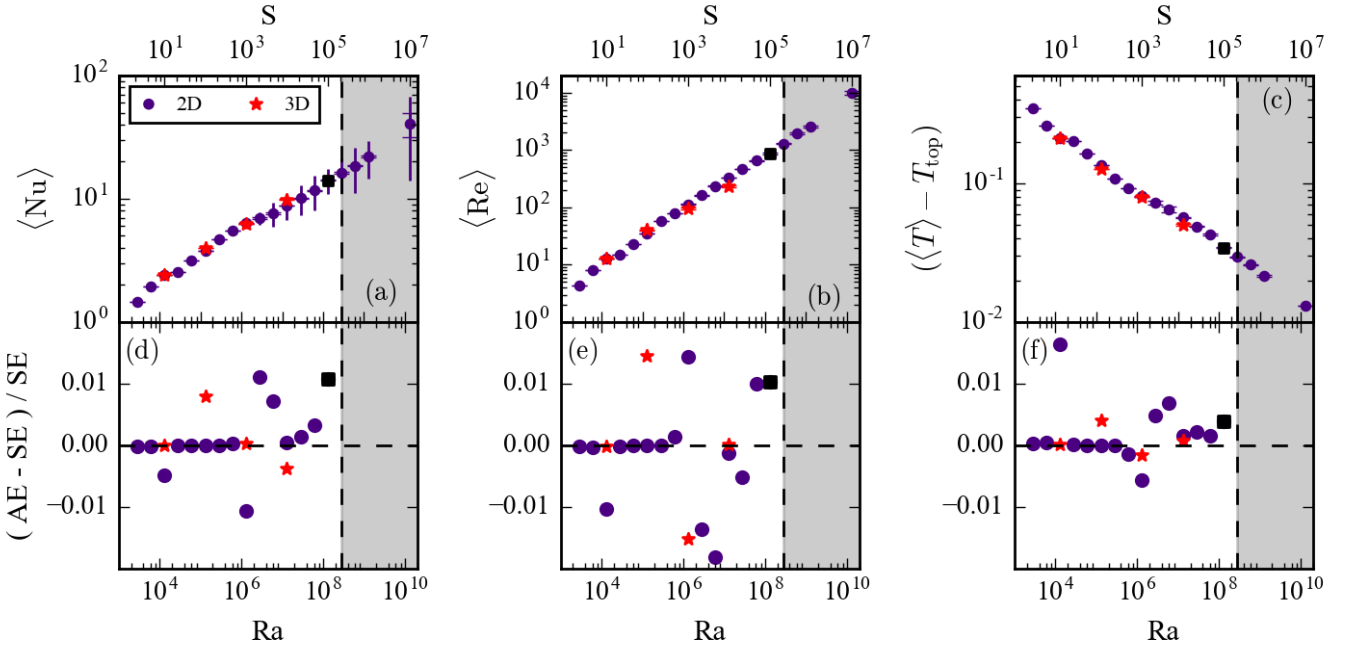


FIG. 2. Volume- and time-averaged measurements of the Nusselt number (Nu), the RMS Reynolds number (Re), and the mean temperature ($\langle T \rangle$) for AE runs are shown in (a)-(c). Symbols are located at the mean value of each measurement. Vertical lines represent the standard deviation of the measurement, and quantify natural variation over the averaging window. Error bars represent the change in the mean value over the averaging window, such that very large error bars represent solutions which are not fully converged when averaging begins. (a) Nu scales as $\mathrm{Ra}^{1/5}$; above $S \geq 10^{3+2/3}$, simulations exhibit oscillating plume structures whose heat transport fluctuates over time. (b) Re, which measures the level of turbulence in the evolved solution, scales as $\mathrm{Ra}^{0.45}$. (c) The difference between $\langle T \rangle$ and the value of $T$ at $z = +1/2$ is shown, and this quantity scales as $\mathrm{Ra}^{-1/5}$, the inverse of Nu. Relative error for measurements of (d) Nu, (e) Re, and (f) $T$ between AE solutions and SE solutions are shown. The greyed area of the plots indicates the region in which only AE runs were carried out due to computational expense. The run at $S = 10^5$ marked as a black square is examined in more details in Figs. 1, 3, & 4.

marginally greater error, with AE measurements being $\leq 2\%$ different from SE measurements.

The measurements presented in Fig. 2 demonstrate that AE can be powerfully employed in parameter space studies in which large numbers of simulations are compared in a volume-averaged sense. We now turn our examination to a more direct comparison of AE and SE for convection at $S = 10^5$, the time and flux evolution of which was shown in Fig. 1. All comparisons that follow for these two runs occur over the times shaded in green in Fig. 1a&c. Measurements are sampled every 0.1 freefall time units for 500 total time units.

As AE is fundamentally a 1D adjustment to the thermodynamic structure of the solution, we compare the horizontally- and time-averaged temperature profiles attained by AE and SE in Fig. 3a. The boundary layer width and structure are nearly identical between the two solutions, but the the mean temperature in the isothermal interior differs by roughly 0.5% (Fig. 3c).

The probability distribution functions (PDFs) of point-by-point temperature measurements are compared for the two runs in Fig. 3b. To construct these PDFs, we interpolate the temperature field of each of these snapshots onto an evenly spaced grid, determine the frequency distribution of all measured $T$ values, and then normalize the distribution such that its integral is unity. The two PDFs have noticeably different modes, as is expected from Fig. 3a. Over long timescales, the 0.5% difference between the two profiles would disappear, as the AE solution evolves to be exactly the SE solution – this is evident in the asymmetry of the AE PDF in Fig. 3b and also the trend of the mean temperature over time in Fig. 3c.

One means of comparing two PDFs to determine if they are drawn from the same underlying sample distribution is through the use of a Kolmogorov-Smirnov (KS) [25]. In general, a KS test must be conducted on independent, uncorrelated data, which poorly describes the point-by-point values of flows in a fluid simulation. Thus, we cannot directly use a KS test to determine if the two fluid samples are the same, but we can draw insight from the profile $\mathrm{KS} = \mathrm{CDF}_{\mathrm{AE}} - \mathrm{CDF}_{\mathrm{SE}}$, where CDF stands for cumulative distribution function, the integral of the PDF. A traditional Kolmogorov-Smirnov statistic is the maximum of the absolute value of the KS profile. We show the KS profile in Fig. 3d, and the CDFs used to construct it overlay the PDFs in Fig. 3b. Near the modes of the temperature PDFs, the KS profile has a maximum value of 0.495, which is very large and implies that roughly half of all temperature measurements in the SE case are greater than those in the AE case. This difference is significant, and shows that the two PDFs are distinctly different, but aside from this large value near the modes the KS profile has very small values, indicating that the temperature fluctuations away from the modes in the two cases are nearly identical.

In addition to comparing the thermodynamic state achieved by the SE and AE methods, we examine the velocities
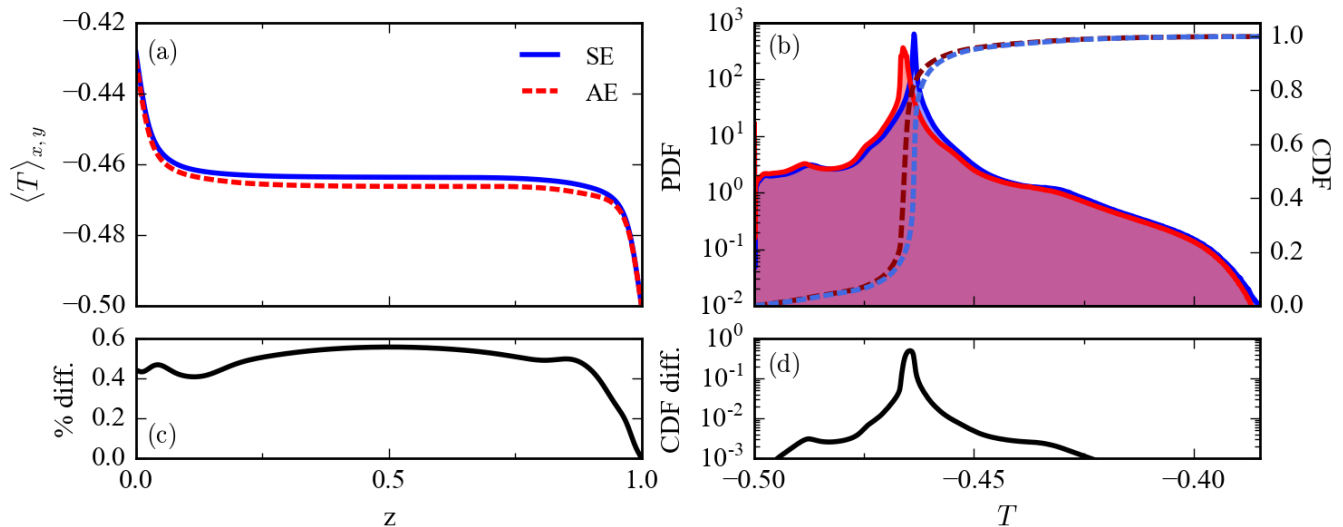


FIG. 3. Comparisons of the evolved thermodynamic states of an AE and SE run at $S = 10^5$ are shown. (a) Evolved horizontally- and time-averaged temperature profiles, as a function of height. (b) Probability Distribution Functions (PDFs) and their integrated Cumulative Distribution Functions (CDFs) of point-by-point measurements of the temperature field. $T$ is sampled every 0.1 time units for 500 total time units, and was interpolated onto an evenly spaced grid before sampling. (c) The percentage difference between the mean temperature profiles as a function of height. The difference between the mean profiles is very small, O(0.5%). (d) The value of the Kolmogorov-Smirnov (KS) statistic, or the difference between the AE and SE CDFs, as a function of temperature. The small difference in the interior temperature results in a large difference between the two temperature CDFs near the values of the temperature modes. The spread of temperature around the modes, which includes the fluctuations that drive convection, are nearly identical between the two runs.
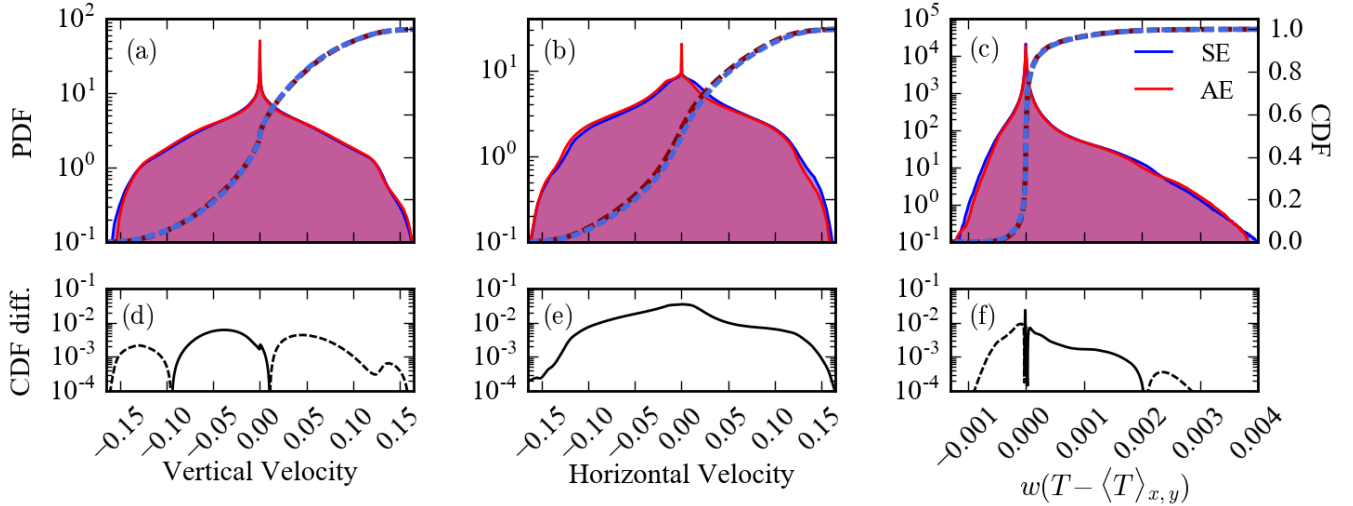
FIG. 4. Probability distribution functions (PDFs) of (a) the vertical velocity, (b) the horizontal velocity, and (c) nonlinear convective transport are shown for 2D runs achieved through SE (blue) and AE (red) at $S = 10^5$. Flows are sampled every 0.1 time units for 500 total time units, and are first interpolated onto an evenly spaced grid. The cumulative distribution function (CDF) is overplotted for each PDF. (d-f) The KS statistics, or the values of $\text{CDF}_{\text{AE}}$ - $\text{CDF}_{\text{SE}}$, are shown for the related distributions, and solid lines indicated positive values while dashed lines are negative values. Unlike the temperature distributions in Fig. 3, these distributions, particularly the vertical velocity and transport, show very good agreement and small values of the KS statistic.

found in the evolved states. Shown are the PDFs of vertical velocity (Fig. 4a), horizontal velocity (Fig. 4b), and the nonlinear vertical convective flux (Fig. 4c). The CDFs of each profile are overplotted, and corresponding KS profiles are shown in Fig. 4d-f. The maximum absolute values of the KS profiles of vertical velocity, horizontal velocity, and nonlinear vertical convective flux are 0.00615, 0.0349, and 0.0263, respectively. Each PDF here shows a strong peak near zero due to the no-slip, impenetrable velocity boundary conditions (Eqn. (7)). The difference in vertical velocity and heat transport is negligible, which is unsurprising in light of the Nu measurements of Fig. 2a&d. The horizontal velocity shows some small deviation between the two simulations, and this likely relates to the nature of the strength of the horizontally oscillatory motions as we previously described in the context of suppressed Nu scaling. Thus, while the temperature profiles are distinctly drawn from different distributions in Fig. 3b, the profiles are similar enough that they drive nearly identical nonlinear dynamics.

The small differences between the SE and AE solutions for the case studied in Figs. 1, 3, & 4, show the extreme power of AE. In addition to the fact that AE runs require much less total simulation time (see e.g., Fig. 1a&c and the time values in the green highlighted regions), the first application of AE in a given simulation (Fig. 1c, at the arrow labeled "1") drastically increases the average timestep by immediately progressing the simulation into a more converged state. For the $S = 10^5$ case we examined in detail, the average time step size grew by a factor of 2-3 due to the decreased convective velocities from the transient state to the evolved state. At $S = 10^7$, the AE solve immediately improved the timestep size by nearly a factor of 4. Thus, AE achieves converged solutions in few simulation time units, while also taking less real world time per simulation time unit, when compared to the slowly converging SE state at the same simulation time.

## IV.   EXTENSIONS & CONCLUSION

In this work we have studied a method of Accelerated Evolution (AE) which can be employed to achieve rapid thermal convergence of convective simulations. We compared this technique to the Standard Evolution (SE) of convection through a thermal diffusion timescale and showed that AE rapidly obtains solutions whose dynamics are similar to SE solutions. The AE method is not only valid at low values of $S$, where SE solutions converge quickly due to the short thermal timescale, but AE is also applicable at high values of $S$, where SE solutions are intractable. We have studied the AE method in both 2D and 3D, but restricted most of our study to 2D flows; AE depends only on 1D, horizontally averaged profiles of dynamics, and our inclusion of 3D simulations was merely to demonstrate the broadly useful nature of AE.

Here we studied Rayleigh-Bénard convection as a test case for the AE method, but we argue that the true power of this technique is in its extensions to more complicated studies. To achieve AE in more complicated systems, one need only derive the steady-state, horizontally-averaged equations governing the convective dynamics (e.g., Eqns. (9) & (10)) and couple those equations with knowledge of the boundary conditions and current dynamics as described in section II A and appendix A. While in-depth studies of AE extensions are beyond the scope of this paper, we will briefly discuss avenues in which the AE method should be explored and tested.

Convection in natural systems is often driven by internal heating processes rather than imposed, fixed boundary conditions. The AE procedure can be straightforwardly applied to Boussinesq studies of internally heated convection [26], where a constant source term in the energy equation causes the vertical flux through the system to increase with height. These systems can be studied using exactly the methods that we examined here, but multiplying the flux profiles derived in Eqn. (8) by the proper, height-dependent flux. Studies of convection in natural system often employ height-dependent conductivities [27, 28], leading to natural flux divergences that act as internal heating terms. The study of AE method in the context of simple internal heating simulations will be an important step towards achieving AE in simulations with astrophysically realistic conductivities.

A further area which could benefit from AE is overshooting convection, in which studies examine adjacent stable and convecting regions [13, 14, 16]. When the interface between the stable region and the convecting region is stiff and motions do not cross that interface, convective motions cannot accelerate the restratification of the stable region. In fully-convective domains, such as those studied in this work, the thermodynamics evolve at a more rapid rate than the thermal diffusion time across the domain due to the help of convective motions. For example, in Fig. 1a, the SE solution is fully converged after $4 \cdot 10^3$ frefall time units, despite the thermal timescale being roughly $10^4$ freefall units. However, in studies where there is a stable region which is not mixed by convection, the experimentalist must either wait through a thermal diffusion time for the region to restratify or employ other methods [13] to study evolved atmospheres.

Studies of stratified, compressible convection have much to gain through developing and employing AE. In many studies of stratified convection, the thermal diffusivity is inversely proportional to the density [7]. Thus, the thermal timescale grows with depth in the atmosphere, and the difficulty of achieving thermal convergence grows as simulators study more highly stratified domains. In order to extend AE into this regime, two additional pieces of information must be considered. First, rather than constructing the profiles in Eqn. (8) with the total flux through the domain, only the superadiabatic portion of the flux should be considered. Second, in addition to solving for hydrostatic balance and thermal equilibrium, as in Eqns. (9) & (10), it is essential to simultaneously evolve the density profile in a manner which conserves mass. In a 1D boundary value problem, such as is solved to achieve AE here, this implies the inclusion of an equation which tracks the vertically integrated mass, and sets boundary conditions on that mass to ensure that no mass enters or leaves the domain.

An eventual use case of AE is in robustly describing convection in stellar evolution codes. Current state of the art stellar structure models are the solutions of 1D simulations which parameterize convection using Mixing Length Theory [29]. Recent work has taken first steps towards understanding how to simultaneously resolve convective motions while evolving systems through many thermal timescales, as is required when modeling the evolution of stars over the course of stellar lifetimes. We now know that implicit timestepping methods, while not technically bound by CFL constraints, must resolve the convective motions for stability [3–5], and are thus not an ideal solution to achiving long-term system evolution. Recently, efforts have begun to project the results of 3D simulations into 1D models to more properly parameterize convection for stellar evolution [30, 31]. Through the careful addition and testing of new physics, AE can be generally applied to very large complex problems such as stellar evolution, and shows great potential for improving our understanding of convection.

## Appendix A: Accelerated Evolution Recipe

In order to achieve Accelerated Evolution (AE), we pause the Direct Numerical Simulation (DNS) which is evolving the dynamics of convection and solve a 1D Boundary Value Problem (BVP) consisting of Eqns. (9) & (10). After

solving this BVP, we appropriately adjust the fields being evolved in the DNS towards their evolved state, and then we continue running the now-evolved DNS. The specific steps taken in completing the AE method are as follows:

1. Wait some time, $t_{\text{transient}}$, before beginning the AE process.

2. During the DNS, calculate time averages of the 1D profiles of $F_{\text{conv}}$, $F_{\text{tot}}$, and $\langle \boldsymbol{u} \times \boldsymbol{\omega} \rangle_{x,y}$, updating them every timestep. To calculate these averages, we use a trapezoidal-rule integration in time, and then divide by the total time elapsed over which the average is taken.

3. Pause the DNS once the averages are sufficiently converged. To ensure that an average is converged, at least some time $t_{\text{min}}$ must have passed since the average was started to ensure that the full range of convective dynamics are probed, and the profiles must change by no more than $P\%$ on a given timestep.

4. Construct $F_{\text{conv, ev}}$ and $\xi$ as specified in section II A from the averaged profiles.

5. Solve the BVP for $\langle T_1 \rangle_{x,y}$ and $\langle \varpi \rangle_{x,y}$ of the evolved state. Set the horizontal average of the current DNS thermodynamic fields equal to the results of the BVP.

6. Multiply the velocity field and the temperature fluctuations, $T - \langle T \rangle_{x,y}$, by $\sqrt{\xi}$ in the DNS to properly reduce the convective flux.

7. Continue running the DNS

We refer to this process as an "AE BVP solve."

While the use of a single AE BVP solve rapidly advances the convecting state to one that is closer to the evolved state, we find that repeating this method multiple times is the best way to ensure that the AE solution is truly converged. For all runs in 2D at $S < 10^5$, we set $t_{\text{transient}} = 50$, completed an AE BVP solve with $t_{\text{min}} = 30$ and $P = 0.1$, and then repeated the procedure. For all 3D runs and 2D runs with $S \in [10^5, 10^6]$, we did a first AE BVP solve with $t_{\text{transient}} = 20$, $t_{\text{min}} = 20$, and $P = 1$ in order to quickly reach a near- converged state and vastly increase our timestep size. After this first solve, we completed two AE BVP solves, with $t_{\text{transient}} = 30$, $t_{\text{min}} = 30$, and $P = 0.1$ to get very close to the solution (as in Fig. 1c). At very high $S = 10^7$, we ran two AE BVP solves with $t_{\text{min}} = 20$ and $P = 1$. For the first solve, we set $t_{\text{transient}} = 20$, and for the second we set $t_{\text{transient}} = 30$. We used fewer solves at this high value of $S$ in part to reduce the computational expense of the run, and in part because a third BVP generally did not greatly alter the solution (as in Fig. 1c, arrow 3).

## Appendix B: Table of Runs

In Table I we list key properties of all simulations conducted in this work. The supercriticality, Rayleigh number, and resolution are reported. We report the simulation run time required to reach a converged state for the SE solutions (one thermal time) and AE solutions, as well as the amount of time over which average measurements were taken once the simulations were converged, in freefall time units. The volume-averaged Nusselt number of the AE and SE solutions are shown. In the upper part of the table, information pertaining to 2D runs is reported, and below the double horizontal bars we report properties of all 3D runs.

[1] B. P. Brown, M. K. Browning, A. S. Brun, M. S. Miesch, and J. Toomre, "Persistent Magnetic Wreaths in a Rapidly Rotating Sun," Astrophys. J. **711**, 424–438 (2010), arXiv:1011.2831 [astro-ph.SR].
[2] N. A. Featherstone and B. W. Hindman, "The Spectral Amplitude of Stellar Convection and Its Scaling in the High-Rayleigh-number Regime," Astrophys. J. **818**, 32 (2016), arXiv:1511.02396 [astro-ph.SR].
[3] M. Viallet, I. Baraffe, and R. Walder, "Towards a new generation of multi-dimensional stellar evolution models: development of an implicit hydrodynamic code," Astronomy & Astrophysics **531**, A86 (2011), arXiv:1103.1524 [astro-ph.IM].
[4] M. Viallet, I. Baraffe, and R. Walder, "Comparison of different nonlinear solvers for 2D time-implicit stellar hydrodynamics," Astronomy & Astrophysics **555**, A81 (2013), arXiv:1305.6581 [astro-ph.SR].
[5] M. Viallet, T. Goffrey, I. Baraffe, D. Folini, C. Geroux, M. V. Popov, J. Pratt, and R. Walder, "A Jacobian-free Newton-Krylov method for time-implicit multidimensional hydrodynamics. Physics-based preconditioning for sound waves and thermal diffusion," Astronomy & Astrophysics **586**, A153 (2016), arXiv:1512.03662 [astro-ph.IM].
[6] D. Lecoanet, B. P. Brown, E. G. Zweibel, K. J. Burns, J. S. Oishi, and G. M. Vasil, "Conduction in Low Mach Number Flows. I. Linear and Weakly Nonlinear Regimes," Astrophys. J. **797**, 94 (2014), arXiv:1410.5424 [astro-ph.SR].

TABLE I. Simulation parameters

| $S$ | Ra | nz | nx, ny | $t_{\text{therm}}$ | $t_{\text{AE}}$ | $t_{\text{avg}}$ | $\text{Nu}_{\text{SE}}$ | $\text{Nu}_{\text{AE}}$ |
|---|---|---|---|---|---|---|---|---|
| $10^{1/3}$ | $2.79 \cdot 10^3$ | 32 | 64 | 52.8 | — | 100 | 1.46 | 1.46 |
| $10^{2/3}$ | $6.01 \cdot 10^3$ | 32 | 64 | 77.6 | — | 100 | 1.95 | 1.95 |
| $10^1$ | $1.30 \cdot 10^4$ | 32 | 64 | 114 | — | 100 | 2.43 | 2.42 |
| $10^{1+1/3}$ | $2.79 \cdot 10^4$ | 32 | 64 | 167 | — | 100 | 2.54 | 2.54 |
| $10^{1+2/3}$ | $6.01 \cdot 10^4$ | 32 | 64 | 245 | — | 100 | 3.14 | 3.14 |
| $10^2$ | $1.30 \cdot 10^5$ | 64 | 128 | 360 | 326 | 100 | 3.8 | 3.8 |
| $10^{2+1/3}$ | $2.79 \cdot 10^5$ | 64 | 128 | 528 | 248 | 100 | 4.71 | 4.71 |
| $10^{2+2/3}$ | $6.01 \cdot 10^5$ | 64 | 128 | 776 | 251 | 100 | 5.5 | 5.5 |
| $10^3$ | $1.30 \cdot 10^6$ | 128 | 256 | $1.14 \cdot 10^3$ | 268 | 200 | 6.4 | 6.33 |
| $10^{3+1/3}$ | $2.79 \cdot 10^6$ | 128 | 256 | $1.67 \cdot 10^3$ | 247 | 500 | 6.87 | 6.95 |
| $10^{3+2/3}$ | $6.01 \cdot 10^6$ | 256 | 512 | $2.45 \cdot 10^3$ | 275 | 500 | 7.54 | 7.59 |
| $10^4$ | $1.30 \cdot 10^7$ | 256 | 512 | $3.60 \cdot 10^3$ | 301 | 500 | 8.83 | 8.83 |
| $10^{4+1/3}$ | $2.79 \cdot 10^7$ | 256 | 512 | $5.28 \cdot 10^3$ | 317 | 500 | 10.13 | 10.14 |
| $10^{4+2/3}$ | $6.01 \cdot 10^7$ | 256 | 512 | $7.76 \cdot 10^3$ | 326 | 500 | 11.65 | 11.69 |
| $10^5$ | $1.30 \cdot 10^8$ | 512 | 1024 | $1.14 \cdot 10^4$ | 411 | 500 | 14.02 | 14.18 |
| $10^{5+1/3}$ | $2.79 \cdot 10^8$ | 512 | 1024 | $1.67 \cdot 10^4$ | 391 | 500 | — | 16.21 |
| $10^{5+2/3}$ | $6.01 \cdot 10^8$ | 512 | 1024 | $2.45 \cdot 10^4$ | 453 | 500 | — | 18.58 |
| $10^6$ | $1.30 \cdot 10^9$ | 1024 | 2048 | $3.60 \cdot 10^4$ | 436 | 500 | — | 22.13 |
| $10^7$ | $1.30 \cdot 10^{10}$ | 2048 | 4096 | $1.14 \cdot 10^5$ | 183 | 200 | — | 40.78 |
| $10^1$ | $1.30 \cdot 10^4$ | 32 | 64×64 | 114 | 261 | 100 | 2.42 | 2.42 |
| $10^2$ | $1.30 \cdot 10^5$ | 64 | 128×128 | 360 | 249 | 100 | 3.97 | 4 |
| $10^3$ | $1.30 \cdot 10^6$ | 128 | 256×256 | $1.14 \cdot 10^3$ | 243 | 500 | 6.27 | 6.27 |
| $10^4$ | $1.30 \cdot 10^7$ | 256 | 512×512 | $3.60 \cdot 10^3$ | 244 | 500 | 9.92 | 9.88 |

[7] E. H. Anders and B. P. Brown, "Convective heat transport in stratified atmospheres at low and high Mach number," Physical Review Fluids **2**, 083501 (2017), arXiv:1611.06580 [physics.flu-dyn].

[8] B. Bordwell, B. P. Brown, and J. S. Oishi, "Convective Dynamics and Disequilibrium Chemistry in the Atmospheres of Giant Planets and Brown Dwarfs," Astrophys. J. **854**, 8 (2018), arXiv:1802.03026 [astro-ph.EP].

[9] M. Stix, "On the time scale of energy transport in the sun," Solar Physics **212**, 3–6 (2003).

[10] H. Johnston and C. R. Doering, "Comparison of Turbulent Thermal Convection between Conditions of Constant Temperature and Constant Flux," Phys. Rev. Lett. **102**, 064501 (2009), arXiv:0811.0401 [physics.flu-dyn].

[11] R. Verzicco and R. Camussi, "Transitional regimes of low-Prandtl thermal convection in a cylindrical cell," Physics of Fluids **9**, 1287–1295 (1997).

[12] N. E. Hurlburt, J. Toomre, and J. M. Massaguer, "Two-dimensional compressible convection extending over multiple scale heights," Astrophys. J. **282**, 557–573 (1984).

[13] L.-A. Couston, D. Lecoanet, B. Favier, and M. Le Bars, "Dynamics of mixed convective-stably-stratified fluids," Physical Review Fluids **2**, 094804 (2017), arXiv:1709.06454 [physics.flu-dyn].

[14] A. Brandenburg, K. L. Chan, Å. Nordlund, and R. F. Stein, "Effect of the radiative background flux in convection," Astronomische Nachrichten **326**, 681–692 (2005), astro-ph/0508404.

[15] R. J. A. M. Stevens, D. Lohse, and R. Verzicco, "Prandtl and Rayleigh number dependence of heat transport in high Rayleigh number thermal convection," Journal of Fluid Mechanics **688**, 31–43 (2011), arXiv:1102.2307 [physics.flu-dyn].

[16] N. E. Hurlburt, J. Toomre, and J. M. Massaguer, "Nonlinear compressible convection penetrating into stable layers and producing internal gravity waves," Astrophys. J. **311**, 563–577 (1986).

[17] E. A. Spiegel and G. Veronis, "On the Boussinesq Approximation for a Compressible Fluid." Astrophys. J. **131**, 442 (1960).

[18] F. Cattaneo, N. H. Brummell, J. Toomre, A. Malagoli, and N. E. Hurlburt, "Turbulent compressible convection," Astrophys. J. **370**, 282–294 (1991).

[19] L. Korre, N. Brummell, and P. Garaud, "Weakly non-Boussinesq convection in a gaseous spherical shell," Phys. Rev. E **96**, 033104 (2017), arXiv:1704.00817 [physics.flu-dyn].

[20] K. Burns, G. Vasil, J. Oishi, D. Lecoanet, and B. Brown, "Dedalus: Flexible framework for spectrally solving differential equations," Astrophysics Source Code Library (2016), ascl:1603.015.

[21] U. M. Ascher, S. J. Ruuth, and R. J. Spiteri, "Implicit-explicit Runge-Kutta methods for time-dependent partial differential equations," Applied Numerical Mathematics **25**, 151–167 (1997).

[22] David Goluskin, Hans Johnston, Glenn R. Flierl, and Edward A. Spiegel, "Convectively driven shear and decreased heatflux," J. Fluid Mech. **759**, 360–385 (2014).

[23] Guenter Ahlers, Siegfried Grossmann, and Detlef Lohse, "Heat transfer and large scale dynamics in turbulent rayleigh-bénard convection," Rev. Mod. Phys. **81**, 503–537 (2009).

[24] J. Otero, R. W. Wittenberg, R. A. Worthing, and C. R. Doering, "Bounds on Rayleigh Bénard convection with an imposed heat flux," J. Fluid Mech. **473**, 191–199 (2002).

[25] J. V. Wall and C. R. Jenkins, *Practical Statistics for Astronomers, by J. V. Wall , C. R. Jenkins, Cambridge, UK: Cambridge University Press, 2012* (2012).

[26] David Goluskin, *Internally Heated Convection and Rayleigh-Bénard Convection* (Springer International Publishing, 2016).

[27] A. Brandenburg, "Stellar Mixing Length theory with entropy rain," arXiv (2016), arXiv:1504.03189.

[28] P. J. Käpylä, M. Rheinhardt, A. Brandenburg, R. Arlt, M. J. Käpylä, A. Lagg, N. Olspert, and J. Warnecke, "Extended Subadiabatic Layer in Simulations of Overshooting Convection," Astrophys. J. Lett. **845**, L23 (2017), arXiv:1703.06845 [astro-ph.SR].

[29] B. Paxton, L. Bildsten, A. Dotter, F. Herwig, P. Lesaffre, and F. Timmes, "Modules for Experiments in Stellar Astrophysics (MESA)," The Astrophysical Journal Supplement Series **192**, 3 (2011), arXiv:1009.1622 [astro-ph.SR].

[30] W. D. Arnett, C. Meakin, M. Viallet, S. W. Campbell, J. C. Lattanzio, and M. Mocák, "Beyond Mixing-length Theory: A Step Toward 321D," Astrophys. J. **809**, 30 (2015), arXiv:1503.00342 [astro-ph.SR].

[31] A. Cristini, C. Meakin, R. Hirschi, D. Arnett, C. Georgy, and M. Viallet, "Linking 1D evolutionary to 3D hydrodynamical simulations of massive stars," Physica Scripta **91**, 034006 (2016), arXiv:1601.01572 [astro-ph.SR].